metals

MDPI

Article

On the Influence of the Initial Shear Damage to the Cyclic Deformation and Damage Mechanism

Hermawan Agus Suhartono [1,*], Kirman Kirman [1] and Yunan Prawoto [2,*]

[1] PTKS, BRIN, Kawasan Puspiptek Gedung 220, Cisauk, Muncul, Kec. Setu, Kota Tangerang Selatan 15314, Indonesia; prtks@brin.go.id
[2] NHK International Co., 46855 Magellan Drive, Novi, MI 48377, USA
* Correspondence: hagussuhartono@yahoo.co.id (H.A.S.); yunan.prawoto@gmail.com (Y.P.); Tel.: +62-812-9728-2767 (H.A.S.); +1-248-880-8148 (Y.P.)

Abstract: The accuracy and precision of lifetime predictions for cyclically loaded technical components are still lacking. One of the main reasons for the discrepancy between the calculated life time and experimental results is that it is not yet possible to create a model capable of describing the microstructural damage process that occurs in the tested material and to subsequently incorporate this model into the calculation. All of the presently available research results recognize that the growth of microcracks is significantly influenced by the microstructure of the material. In order to take into account the influence of the microstructure on the damage process, research on the very early fatigue damage is carried out. The results are obtained from tension and torsion fatigue testing. For this purpose, the surfaces of the tested specimens are carefully observed to discover and analyze microcracks, which are classified according to their orientation. Moreover, the mechanisms of crack initiation and propagation are major points of interest. Through a mix of mechanical and metallurgical points of view, calculations and multi-level FEA modeling are carried out to gain a better understanding of the properties of the phases. The simulation is based on continuum mechanics, which considers the positions and mechanical metallurgy, which account for each constituent character's failure laws. It is concluded that both the experimental and computational approaches conform, showing that such an approach is indeed a necessity and should become a trend in the near future. Statistically, microcracks under tension modes are highest at 45° (approximately 30%), while under torsion they are highest at 0° (approximately 20%) with respect to the sample orientation. The influence of the microstructure is explained via the finite element analysis.

Keywords: cyclic stress; damage; FEA (Finite Element Analysis); multi-level modeling

Citation: Suhartono, H.A.; Kirman, K.; Prawoto, Y. On the Influence of the Initial Shear Damage to the Cyclic Deformation and Damage Mechanism. *Metals* **2022**, *12*, 1072. https://doi.org/10.3390/met12071072

Academic Editors: Alberto Campagnolo and Alberto Sapora

Received: 17 April 2022
Accepted: 8 June 2022
Published: 23 June 2022

1. Introduction

The accuracy in predicting the ages of components that are subjected to fatigue loading is still far from satisfactory. The causes of deviations between the calculation results and experimental results include a lack of understanding of the process of the damage mechanism that occurs in the material [1,2]. Research in this field has identified that at low loading most of the component life is used for the crack initiation phase [3], while at high loading the component life is used for the crack propagation phase [4,5]. Crack initiation and growth in the early stages are strongly influenced by the microstructure of the material [6–8]. To determine the effect of microstructure on the damage process, a study was carried out on an early stage damage due to fatigue loading.

Component failure due to fatigue has been receiving profound attention from industry, researchers, and academicians. Various methods have been developed to observe the mechanism and behavior of fatigue cracking [7,8]. Various disciplines such as metallurgy, material mechanics, mathematics, and statistics have been used to solve this problem [9], each contributing ideas based on their scientific views, although the unification of the

results from various laboratories on this matter has been missed due to the large amount of published studies. However, the importance of the crack propagation mechanism in fatigue damage has long been recognized [9].

This paper combines three different approaches of testing, simulation, and analysis, with an emphasis on the damage mechanism. Tests are carried out on aluminum with uniaxial tension and torsion fatigue loading. In this test, the surface of the specimen is carefully observed to find and analyze its microcracks. Attention is mainly paid to the mechanism of crack initiation and propagation. The ultimate goal of this research is to incorporate the parameters obtained from this study into the calculation to improve the prediction of the component life. Evaluations of the crack formation and propagation are carried out on an aluminum alloy to gain a better description of the damage process under fatigue loading.

It is widely known that metals are formed in a solid crystalline arrangement. The atoms are arranged in an orderly arrangement of space. The difference in the crystal arrangement lies in the shape and the relationship between each atom. The regularity of the atomic arrangement forms a crystal structure. The simplest structure that describes the crystal structure is a crystal cell [10,11]. Some mechanical properties such as the ability to change shape and the propagation cannot be traced from the shape of this single crystal cell. In a single crystal cell, the distances between atoms in different directions are different. For example, in aluminum metal, the farthest distance is on the space diagonal and the closest distance is on the front diagonal. In steel, the farthest distance is on the front diagonal and the closest distance is on the space diagonal. The difference in atomic distance causes some metal properties to depend on the direction [10,11], although engineering metals generally consist of many heterogeneous crystals. Dislocation movement does not have the same probability in all directions. The shift only occurs in the plane that has the densest atoms. In ferrous metals, there are 4 shear planes that have the greatest atomic density, whereas in aluminum there are 4 shear planes with 3 directions, so there are 12 sliding systems [12]. In polycrystalline materials, each grain has its own shear system, so that when a shift occurs only a few grains have the most favorable orientation.

The paragraph above explains the ideal nanoscale situation, and ideally the computational approach should incorporate these theories. However, such an attempt is almost impossible due to the cumbersomeness of the computational method. Therefore, in this research, the computational approach is limited to accommodating the variation in the mechanical properties of each constituent and their positions relative to each other. Without a doubt, this approach is far from perfect, but it is an early stage in accommodating the microscopical metallurgical theory using a simple finite element analysis.

Meanwhile, grain boundaries have an effect on inhibiting the movement of dislocations. For a grain with a favorable orientation, a critical shear stress is reached, meaning the dislocation can move up to the grain boundary. When the shear stress increases to a certain level, this grain boundary resistance can be passed. To explain the crack propagation across this grain boundary, several models were developed. Zhang [13] stated that cracks prefer to propagate along slip systems with high Schmidt factors when transferring from one grain to another. The Schmidt factor is defined as the ratio of the resolved shear stress on a certain slip system to the applied stress. Cracks generally occur in areas of high stress due to repeated loading. In this study, the experimental results for AlMgSi1 are reported, which was subjected to tension and torsion fatigue loads.

The calculation and modeling were carried out to deepen the understanding of the properties of its phases through a combination of mechanical and metallurgical points of view. The simulation was based on the continuum mechanics while taking into account the mechanical metallurgy of each constituent character with different failure laws, using a conventional finite element analysis.

2. Testing

The experiments were carried out on AlMgSi1 alloy. The material has the potential for strengthening with age. The condition of the material upon receipt showed that the AlMgSi1 was the result of extrusion. Table 1 shows the chemical composition of the material tested. The composition shown in the table is in weight %.

Table 1. Chemical composition (% by weight) of AlMgSi1 alloy.

Element	% Weight	Element	% Weight
Si	0.47	Cr	0.88
Fe	1.11	Zn	0.01
Cu	0.36	Ti	0.10
Mn	0.07	Pb	0.01
Mg	0.74	Al	92.72

2.1. Metallography

Figure 1 shows a picture of the microstructure of the AlMgSi1 alloy in a finely polished state. The first particles to precipitate are clearly visible. These deposits have sizes up to 9 µm. The finer Mg2Si particles that appear as darker dots are distributed in the grains. The alloy has an average grain diameter of 10 µm and there are some grains with a diameter of 40 µm. The first particles to precipitate are accordant with [14–16], whereby a network of coarse Mg_2Si particles is distributed along the grain edges.

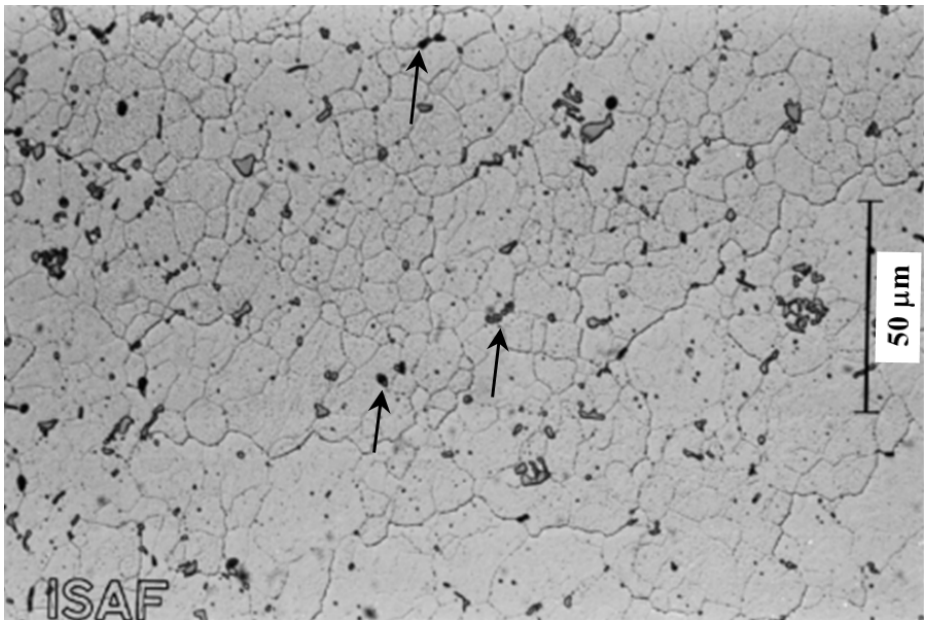

Figure 1. Photo of the microstructure of the AlMgSi1 alloy in a finely polished state. Mg2 Si precipitates are pointed out by arrows. (ISAF is Institut für Schweißtechnik und Trennende Fertigungsverfahren, Germany).

2.2. Transmission Electron Microscopy (TEM)

Transmission electron microscopy (TEM, JEOL, Tokyo, Japan) examinations were conducted on non-aged AlMgSi1 Alloy. The specimens were sent to IWS Dresden, Germany to investigate the state of the alloy thoroughly.

The TEM examination of the non-aging condition of the AlMgSi1 alloy shows the state of the precipitate in the form of the Guinier–Preston–Zonen deposits along the crystallographic direction <100> (see Figures 2 and 3).

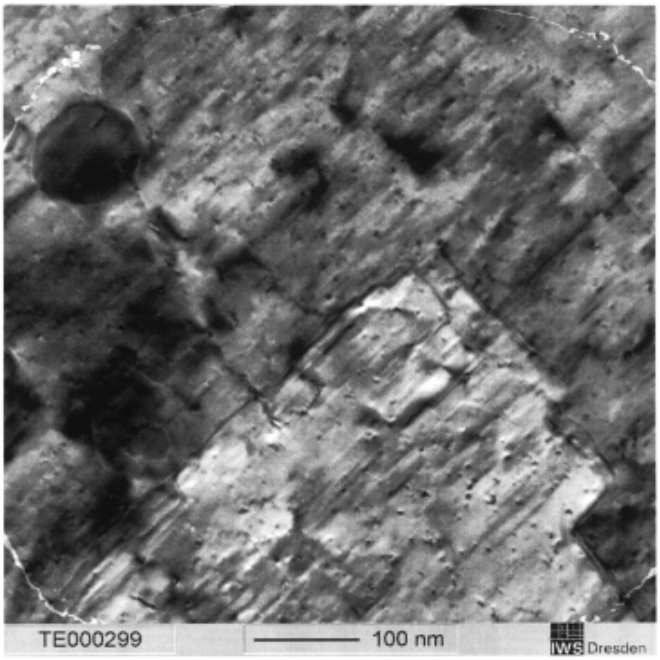

Figure 2. TEM results for the AlMgSi1 alloy in the initial state. Precipitation strengthening in the crystal state.

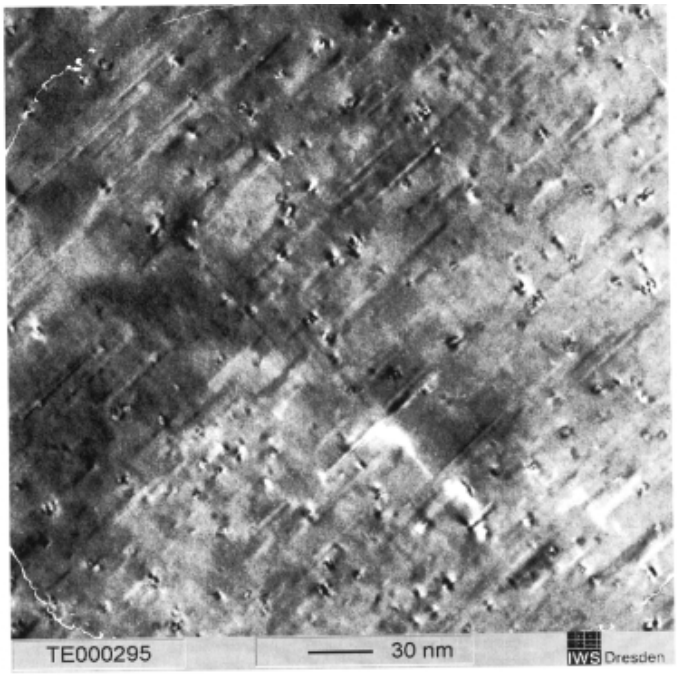

Figure 3. TEM results of the AlMgSi1 alloy as-received (extrusion and cold storage) for two coherent precipitate groups (Guinier–Preston–Zonen), where small particles of precipitate appear in contrast.

2.3. Tensile Test

The determination of the mechanical properties was achieved via tensile testing. The test object was made according to DIN 50125 with a diameter of 6 mm. According to the manufacturer's information, AlMgSi1 (F28–31) has a tensile strength of σ_u = 436 MPa. The tensile strength obtained from the tensile test showed low deviation from the description for the aged condition from the manufacturer. The tensile test characteristics are given in Table 2.

Table 2. Tensile test characteristics of AlMgSi1 alloys.

σ_u (MPa)	$\sigma_{0.2\%}$ (MPa)	A_5 (%)	Z (%)	E (MPa)
437	420	12.2	37.3	86,000

Note: σ_u = ultimate strength; $\sigma_{0.2\%}$ = yield strength; A_5 = elongation; Z = reduction area; E = Young's modulus.

2.4. Hardness Test

Hardness measurements were carried out at room temperature with a test load of 0.49 N and a tracking time of 15 s. Hardness is measured from the center of the outer diameter of 21 measurement points. The average hardness was 124.9 HVN.

2.5. Fatigue Test Program

The material used as the research material was AlMgSi1 alloy with a round cross-section. The test was carried out based on the consideration of the introduction of the material characteristics and the technical use of the material. For fatigue testing, a cylinder with a wall thickness of 1.5 mm was used (stress concentration factor K = 1). The inner and outer sides were finely polished. For fatigue testing, a hollow cylindrical specimen with a wall thickness of 1.5 mm was used (stress concentration 1). The cylinder bore had a diameter of 18 mm. The inside of the test object was carried out by honing, while the outside was sanded and finely polished to eliminate the effects of stress concentration arising from machining, and as much as possible to produce a shiny smooth surface so that microcrack observations could be made. The dimensions of the fatigue specimen are shown in Figure 4 and the polished specimen with a total length of 160 mm is shown in Figure 4. The smoothness of the inner surface is equally important so that the surface is notch-free. If this is neglected then the drill trace will dominate and cracks may develop on the inner wall so that it cannot be observed. Drilling results in a deeper imprint than smooth turning of the surface, so further deep surface machining is required.

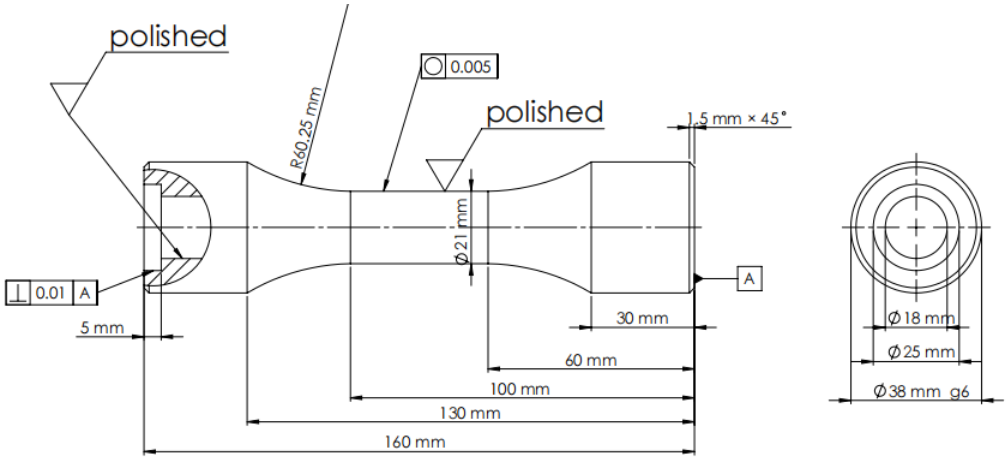

Figure 4. The dimensions of the fatigue specimen.

To achieve the mechanical reinforcement of the inner wall, a fine roller tool was used, which suppressed the former drilling machining, resulting in a strengthening effect. Subsequent polishing produced a surface with a roughness of Ra 0.1 µm. The subsequent fatigue tests showed that after this process, microcracks appeared on the surface, which was a requirement of this study. The surface of the test object also had a roughness of Ra 0.1 µm.

For the experiment, a servo-hydraulic testing machine was developed for compressive tension loading and torsional loading. The test machine was equipped with a separate hydraulic pump. The equipment was interconnected with PCs and controllers. This equipment allows the application of a wide variety of loadings. Measurement values were taken through 2 load cells.

A multi-axis servo-hydraulic test machine for tension–compression and torsional loading was set up for the experiments. The loading is guided by two hydraulic cylinders, while the target value is specified with a special personal computer (PC) software.

The devices are interconnected with the PC and the control unit. This equipment allows the application of a wide variety of loadings. The measured values are recorded through two load cells, two inductive displacement sensors (integrated in the servo-hydraulic cylinder), a torque sensor, and a multi-axis strain displacement sensor (Figure 5), which is passed on to the test bench PC with an integrated analog–digital card.

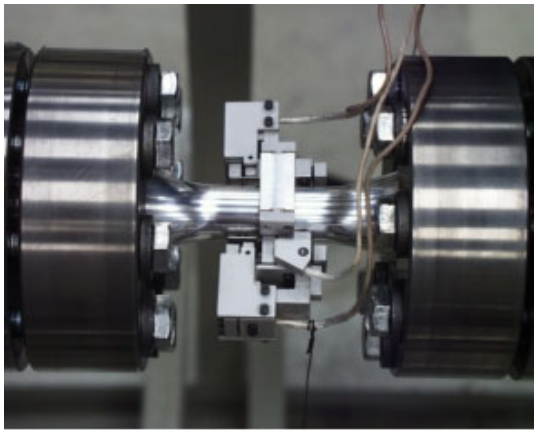

Figure 5. Fatigue test specimen with strain recorder.

The testing was carried out under room temperature. The frequency range of the fatigue tests was 0.5–1 Hz.

3. Test Results and Discussion

3.1. Dynamic Characteristics of Materials

The dynamic stress–strain diagram describes the relationship between the stress and strain amplitudes under cyclic loading at one stress level under saturation conditions. From the obtained hysteresis results, the tensile strain, shear strain, tensile stress, and shear stress can be calculated. From these data, the cyclical Ramberg–Osgood and Coffin–Manson characteristics can be determined. These characteristics are given in Table 3. Axial stress–strain diagrams and strain life diagrams are given in Figures 6 and 7, while torsional stress and strain diagrams and torsional strain life diagrams are given in Figures 8 and 9. The fatigue test showed that under axial compression tensile loading and torsional loading there was no effect of strain hardening or strain softening.

Table 3. Dynamic characteristics of $AlMgSi_1$.

Parameter	Tension Fatigue Testing	Torsion Fatigue Testing
Modulus E	74,499 MPa	-
Modulus G	-	28,822 MPa
ε'_f	0.0967	-
γ'_f	-	2.204
σ'_f	577.560	-
τ'_f	-	263.040
b_σ or b_γ	−0.074	−0.062

Table 3. *Cont.*

Parameter	Tension Fatigue Testing	Torsion Fatigue Testing
b_σ or b_γ	−0.655	−0.894
$n' = \frac{b}{c}$	0.113	0.069
$K' = \frac{\sigma'_f}{\left(\varepsilon'_f\right)^{n'}}$	752.130	249.130

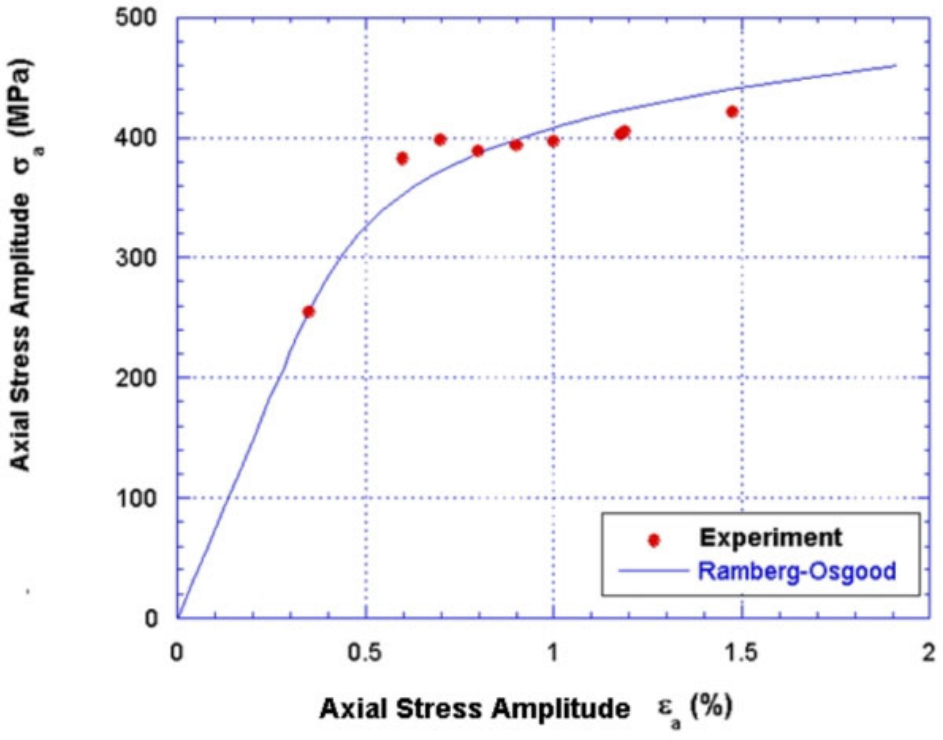

Figure 6. Dynamic stress–strain diagram for AlMgSi1.

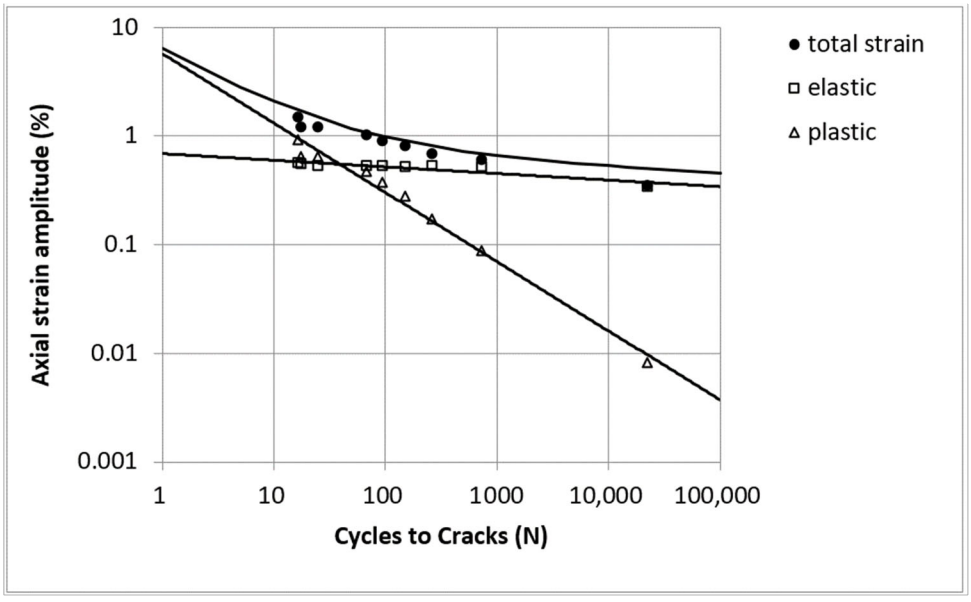

Figure 7. Axial strain life diagram for AlMgSi1.

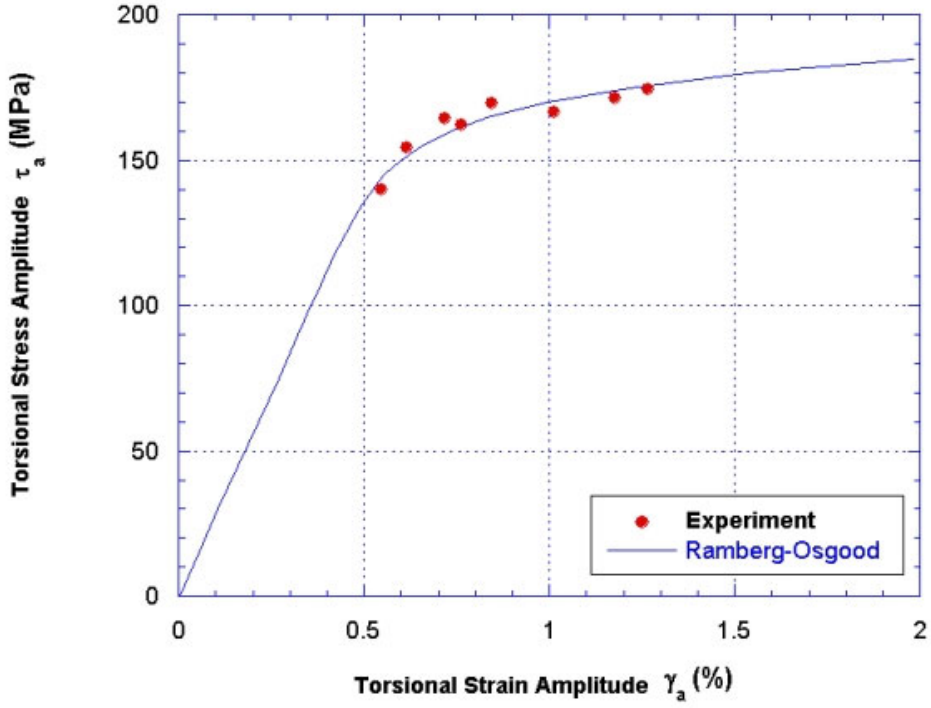

Figure 8. Dynamic shear stress–strain diagram for AlMgSi1.

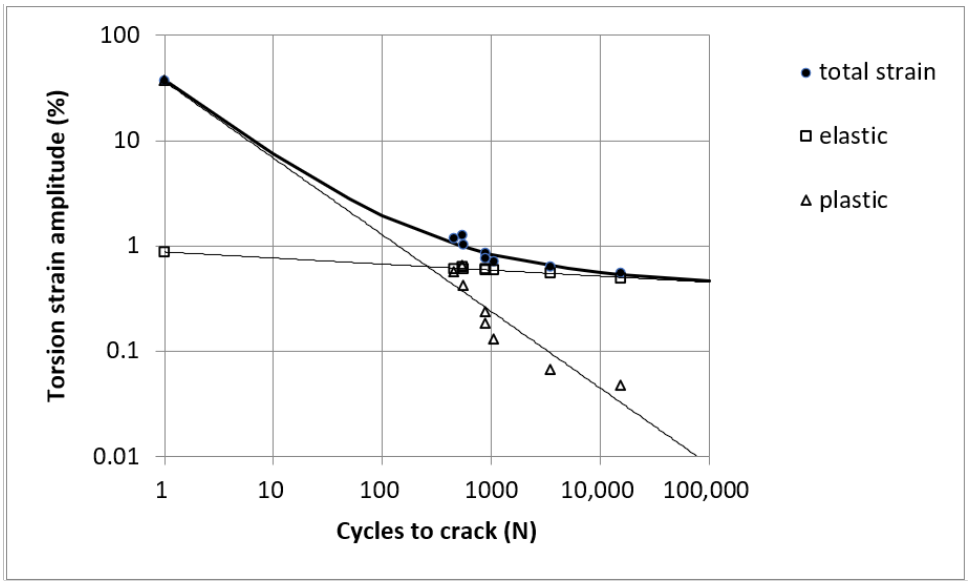

Figure 9. Torsional shear strain life diagram for AlMgSi1.

3.2. Crack Research

In this study, the specimens were loaded for a certain cycle, then the test was stopped and the specimens were examined with an optical microscope for crack examinations, although some of them were examined by SEM. This step was then repeated until a technical crack or fracture occurred. Cylinders that had been loaded were placed on the specimen holder on the observed part and marked until they were recovered for further inspection so that further crack propagation could be investigated qualitatively and quantitatively. The test object was examined in 12 places and magnified 250× (see Figure 10).

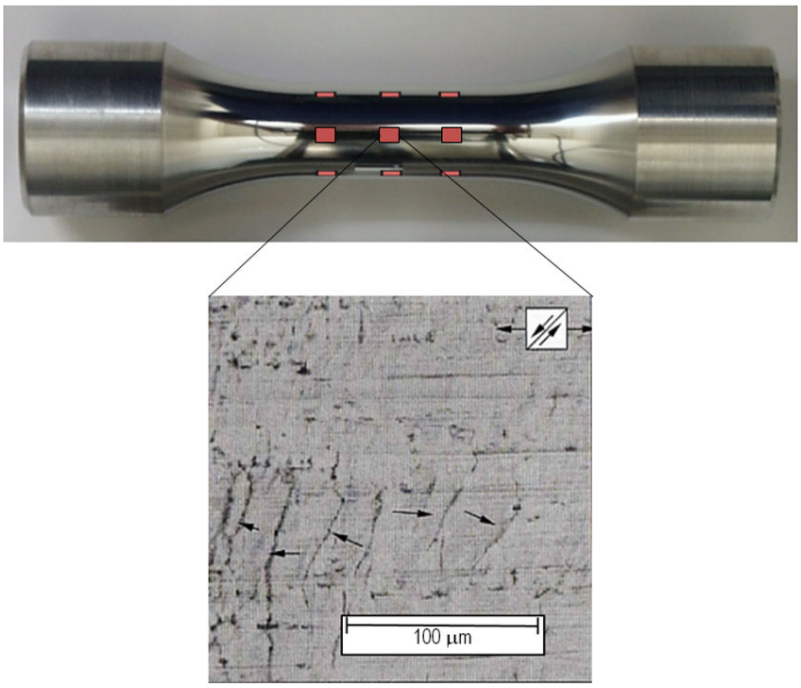

Figure 10. Fatigue test specimens were observed in 12 different places. The surface of the specimen is shown after being loaded with a compressive tensile load, ε_a = 0.6%, N = 600 cycles.

The number and orientation of cracks shown in the microscopic photo of the surface of the specimen were evaluated to determine the characteristics of crack propagation under various loadings. Observations were made on the type of loading so that the distinctiveness of the microcrack due to each loading type could be observed. To assess microcracks, it is necessary to know the general descriptions of the emergence of microcracks, microcrack propagation, and crack coalescence. Because the dynamic loading is in line with the loading frequency, there is a change in the dislocation structure. The dislocation shift causes the surface structure to change. If in one place there is a strong shift with a large enough material shift, extrusion and intrusion will occur [17]. The fatigue life of the material is determined from the microstructure, grain conditions, and crystal orientation. Grain boundaries are an obstacle to microcracking [6,7,13]. The possibility of a microcrack continuing to propagate is determined, among other things, by the orientation of the surrounding crystals and grains. The grain size has an influence on the crack propagation. The smaller the grain boundaries, the cracks that propagate will more often experience grain boundary obstacles, whereby at the grain boundaries the cracks temporarily do not propagate. If the loading at the crack tip, which is a function of the loading conditions and grain orientation, is large enough, then the crack can cross the grain boundary [18]. In addition to crack growth due to the loading of each cycle, crack propagation can also occur due to the connection of two adjacent cracks. If this happens then this phenomenon is called crack coalescence. Figure 11 shows a microscopic image of a surface that has been subjected to torsional loads. The microcracks propagate parallel to the direction of the shear stress.

Figure 11 shows cracks that propagate on the surface. The crack propagates well on the surface (type A crack) but also propagates towards the depth (type B crack) [19], as shown in Figure 12.

SEM Observations

For a more thorough observation of the initiation and propagation of cracks, observations were made with a raster electron microscope, Carl Zeiss AG, Oberkochen Germany. The research was conducted in the area around the fault. The torsion loading shows that

crack initiation starts from the position of the particles (Figure 13a). The holes in the figure are the positions of the particles that are out of place, similar to the non-metallic inclusions that fall due to fatigue cracking.

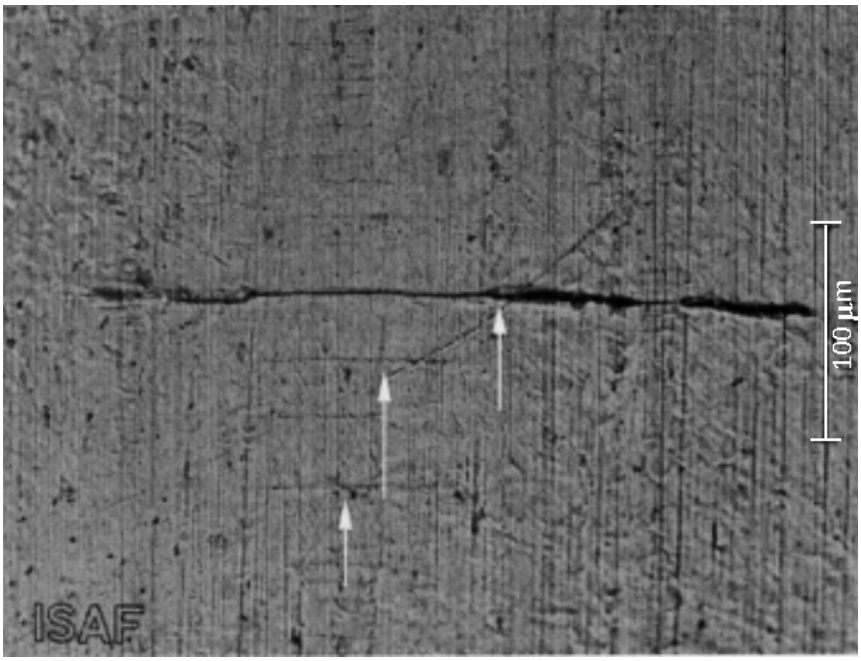

Figure 11. Image of the surface of the AlMgSi1 test object after being given a torsional dynamic load, a = 0.76%, N = 870 cycles, the arrows show the cracks. ISAF is Institut für Schweißtechnik und Trennende Fertigungsverfahren, Germany.

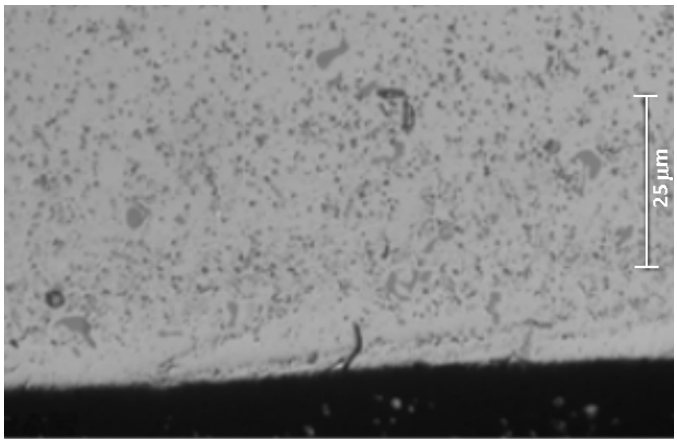

Figure 12. Cracks that radiate inward.

The formation of cracks in these particles is the result of differences in the elastic characteristics between the particles and their matrix. The particles cannot or do not easily plastically deform while the matrix is deformed. This causes the accumulation of dislocations in that location. Several torsion cracks with a crack direction parallel to the orientation of the maximum shear stress are shown in Figure 13b. The cracks are inhibited by microstructural barriers, namely the orientation of the surrounding grains, which conforms to other researcher findings [2,7,13].

Observations with SEM for the test specimens of tension compression fatigue test results are shown in Figure 14. From this figure, it can be recognized that plastic deformation causes the particles to move out of position. Besides this, a microcrack at stage I can be found.

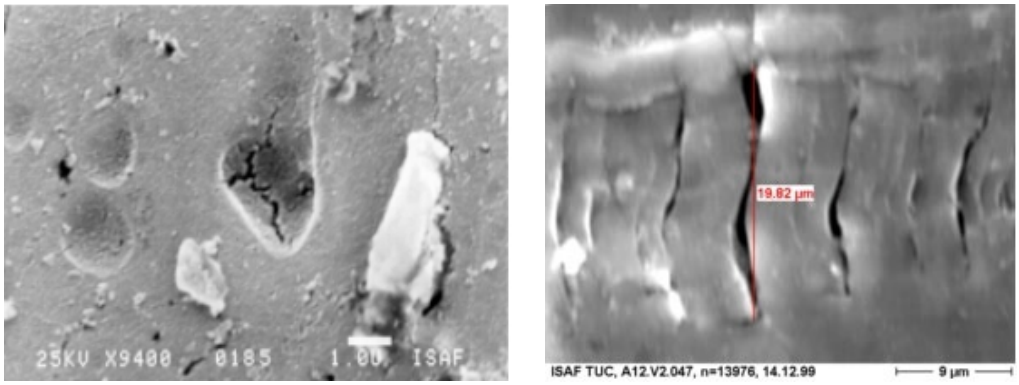

(**a**) (**b**)

Figure 13. SEM image of the surface of the test object due to torsion load, γ_a = 0.55%, N = 13,976. (**a**) crack initiation starting from the position of the particles; (**b**) torsion cracks.

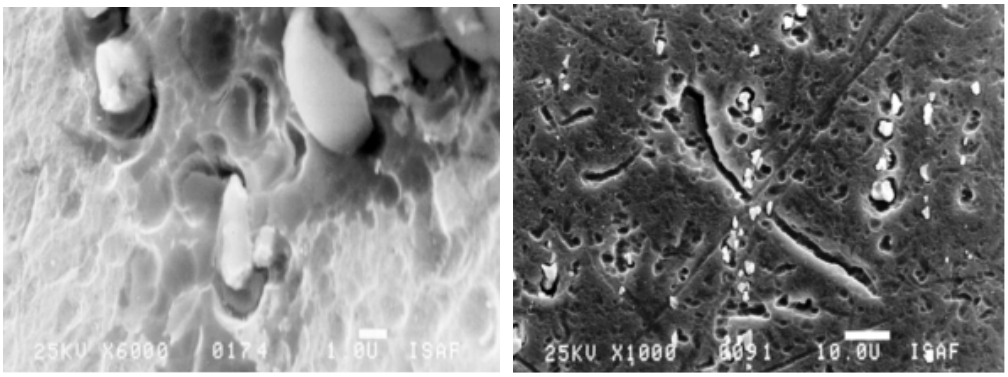

(**a**) (**b**)

Figure 14. SEM results for the test object after being loaded with compressive tension, ε_a =1%, N = 66. (**a**) Particle movement; (**b**) microcrack.

Figure 15 shows the SEM results of the fracture surface after being given a tension compression fatigue load. On the surface of the test object can be found several longer cracks. At a smaller strain amplitude, which means that the loading cycle received by the test object is larger, smaller microcracks can be observed (see Figure 16).

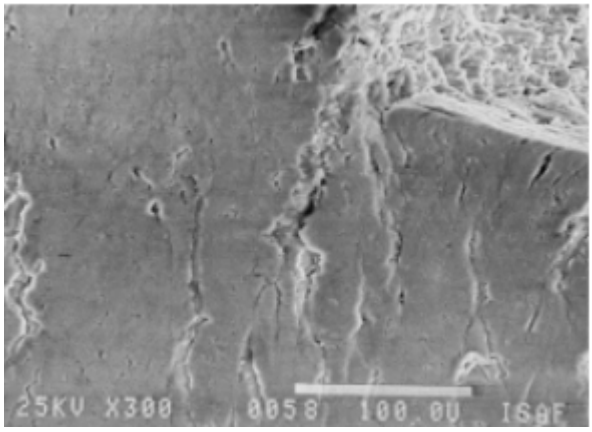

Figure 15. Results of SEM photo of the surface of the test sample, compressive tensile loading with microcracks near the fracture surface, ε_t = 0.6%, N = 100.

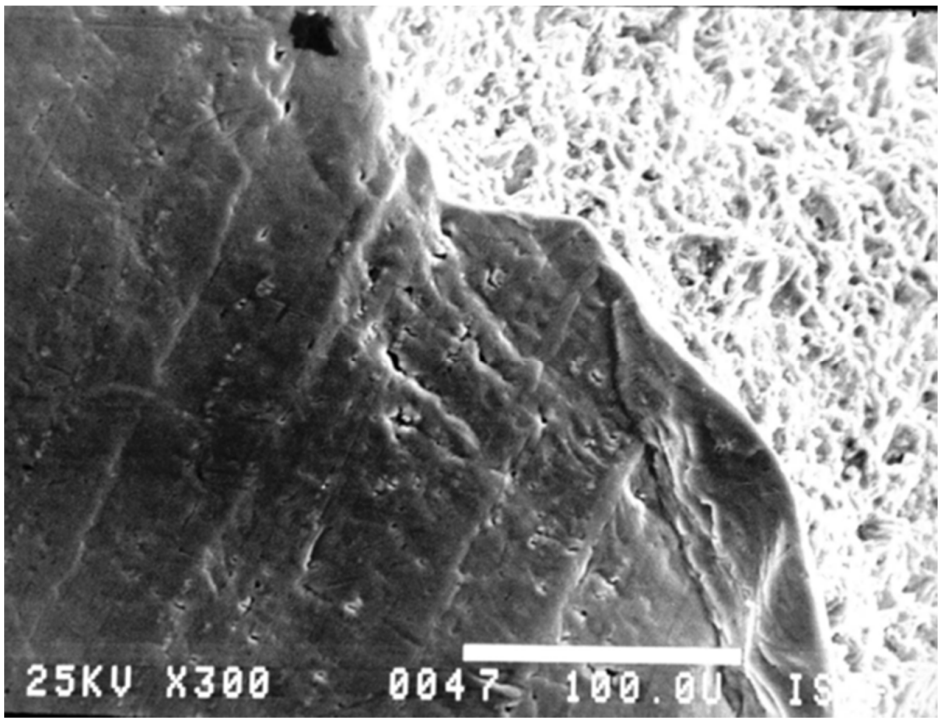

Figure 16. Results of SEM photo of the surface of the test object, compressive tensile loading with microcracks near the fracture surface, t = 0.35%, N = 24,470.

In accordance with the laws of the mechanics of the materials, the loading caused by external forces will cause tensile and shear stresses to the material, which will be transferred to each grain. In the case of tensile loading, the maximum shear stress occurs at an angle of 45° to the direction of the tensile stress and has a magnitude of 1/2 of the tensile stress. Under tensile loading, the maximum shear stress direction is 45°. The distribution of cracks under compressive tensile loading in the experiment spreads at all angles with a tendency toward a direction parallel to the direction of the shear stress, namely ±45°. Figures 10 and 14b show the microcracks of the specimen under fatigue tension compression loading. The microcracks and their orientations are counted and presented in Figure 17. In torsional loading, the directions of the maximum shear stress are 0° and 90°, and the cracks that occur appear to follow those directions (see Figures 11 and 13). The microcracks distribution is shown in Figure 18.

Stage I or the microcrack growth is generally a shear-mode crack that is closely related to the crystal planes. When the stage I crack propagation passes through two grains, a slight change in the orientation of the propagation plane can be observed. Stage I crack propagation may include two or more grains when the shear plane angle difference is low, because the small-angle grain boundaries fail to provide barriers to the crack propagation. Stage II crack propagation or striation crack propagation is known to be a crack propagation mechanism controlled by mode I crack propagation, i.e., the surface of the crack propagation is perpendicular to the maximum principal stress. This is closely related to the difference in shear planes in phase I of the crack propagation (microcrack propagation), so that the transition to phase II crack propagation, as shown in Figures 10 and 19, was found experimentally under tension compression loading. The early part of the stage II propagation still shows surface appearances that show a dependence on the crystal orientation, before the dominant striation mechanism plays an important role [20] The mechanical properties of the metals depend on the crystal structure, crystal defects, and grain dimensions (size and shape of the grains). Macroscopic deformation can be distinguished by changes in length and changes in angle (shear). When the applied force is divided by the surface area, the mechanical stress is obtained. The shear deformation is called the shear stress.

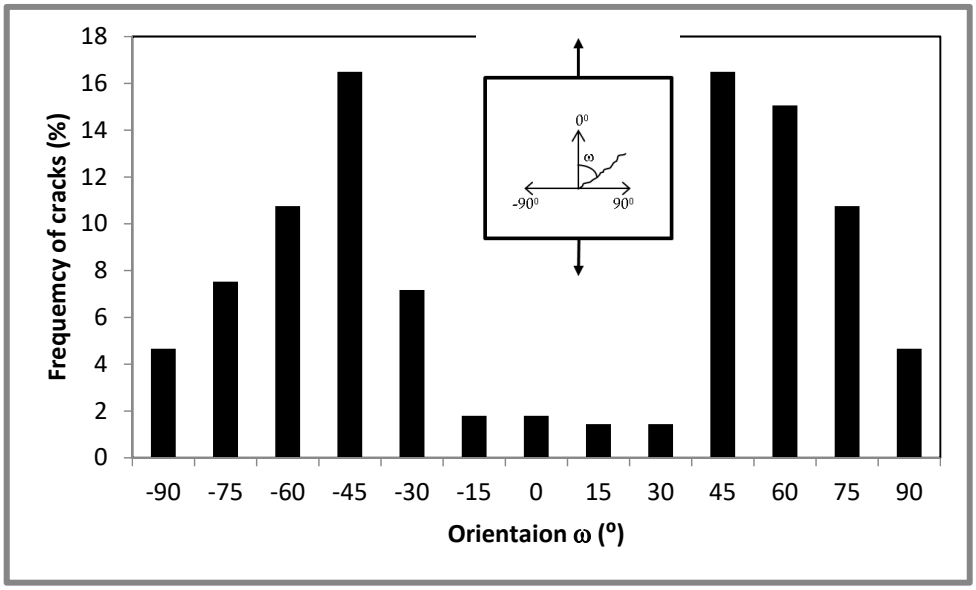

Figure 17. The microcracks and the orientation of the specimen under tension compression loading.

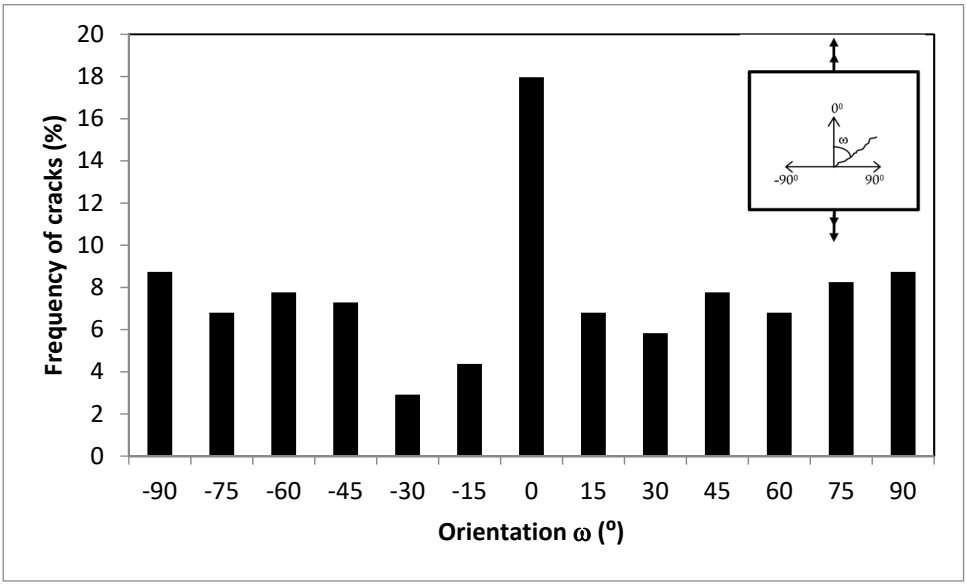

Figure 18. The microcracks and the orientation of the specimen under torsion loading.

In accordance with the laws of mechanics, it can be concluded that upon external loading of each grain, a tensile stress will arise in each grain; at an angle of 45° to this tensile stress, a maximum shear stress will arise, which will have a magnitude of 1/2 of the tensile stress [21].

For a simplified two-dimensional plain strain condition, the principal stresses are:

$$\sigma_{1,2} = \frac{\sigma_x + \sigma_y}{2} \pm \sqrt{\left(\frac{\sigma_x - \sigma_y}{2}\right)^2 + {\tau_{xy}}^2} \quad (1)$$

Here, the maximum shear stress is:

$$\tau_{\max} = \left(\left(\frac{\sigma_x - \sigma_y}{2}\right)^2 + {\tau_{xy}}^2\right)^{\frac{1}{2}} \quad (2)$$

$$\tau_{\max} = \frac{\sigma_1 - \sigma_2}{2} \tag{3}$$

The direction of the principal stress is calculated according to the following formula:

$$\varphi = -\frac{1}{2}\left(\arctan\frac{2\tau_{xy}}{\sigma_x - \sigma_y}\right) \tag{4}$$

The direction of the maximum shear stress is:

$$\phi = \varphi + 45^\circ \tag{5}$$

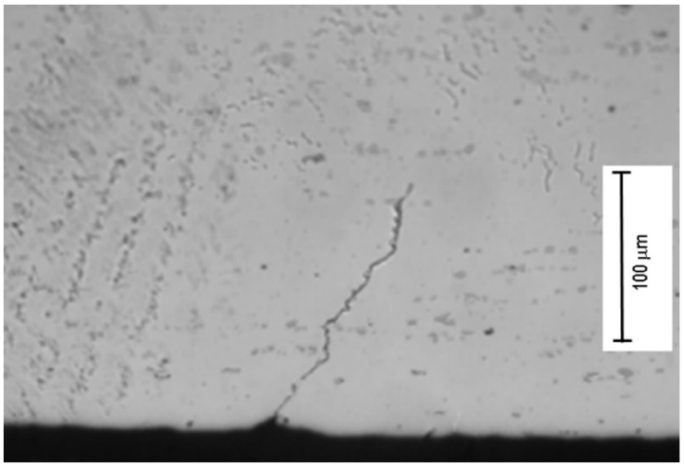

Figure 19. Two stages of fatigue crack propagation.

Under tensile loading, the direction of the maximum shear stress is shown in Equation (5). From the results of the stress calculations, the direction of the maximum shear stress is 45°. The distribution of cracks under compressive tensile loading in the experiment spreads at all angles, with a tendency toward a direction parallel to the direction of the shear stress, which is ±45°.

Under torsional loading, the directions of the maximum shear stress are calculated based on Equation (4), namely 0° and 90°. The experimental results under torsional loading show microcracks that arise with orientations in all directions. with the largest number of cracks in the 0° direction, namely the direction of the maximum shear stress. Stage I or microcrack growth is generally a shear-mode crack that is closely related to the crystal planes. When the stage I crack propagation passes through two grains, a slight change in the orientation of the propagation plane can be observed. Stage I crack propagation may include two or more grains when the shear plane angle difference is low, because the small-angle grain boundaries fail to provide barriers to the crack propagation.

4. Modeling and Simulation

The simulation and modeling were conducted for the purpose of deepening the understanding of the properties of the phases by combining the mechanical and metallurgical perspectives. The focus was on the load capacity and favorable failure conditions based on various failure laws for different constituents. In this study, representatives of the microstructures of aluminum phases were selected. Aluminum AlMgSi1 was used as the basis for the evaluation. The calculated modeling was based on AlMgSi1, but the developed method should be applicable to other similar metals. The Al–Mg–Si alloys, being the alloys of choice for medium-strength architectural and transportation applications, feature most prominently in the automotive industry. The two main alloying elements Mg and Si were included in small amounts (≈1%) to form hardening precipitates, which typically contribute a five-fold strength increase over pure aluminum [22–24]. There is a handful of discovered metastable phases in the Al–Mg–Si system alone. Precipitates form during aging

at medium to high temperatures (around 150 °C) after solution heat treatments (around between 400 and 500 °C). Then, rapid cooling ensures a supersaturated solid solution (SSSS), after which the solutes start clustering in the face-centered cubic Al lattice. The strength is caused by a high number and density of nano-sized, needle-shaped β″ precipitates, usually together with Guinier–Preston (GP) zones. With increasing temperature and aging time, the number density decreases while the precipitates coarsen and are replaced by more stable types. Alloys on the ternary Al-Mg-Si system with the addition of Cu, Fe, Mn, and Cr, among others, possess a precipitation sequence where the supersaturated solid solution is rich in non-equilibrium vacancies that enable a passage through a series of metastable precipitates towards the equilibrium, described as SSSS → clusters → β″ → β′→ β [8–10]. There is also a possibility that the coarse Mg2Si (eutectic) is formed in the AlMgSi alloy. Figure 20 shows a diagram illustrating the possibility of forming coarse eutectic Mg2Si under non-equilibrium conditions. While a more in-depth discussion of each ingredient is not included, the primary factors that influence the load-carrying capacity are briefly reviewed for the reader's convenience.

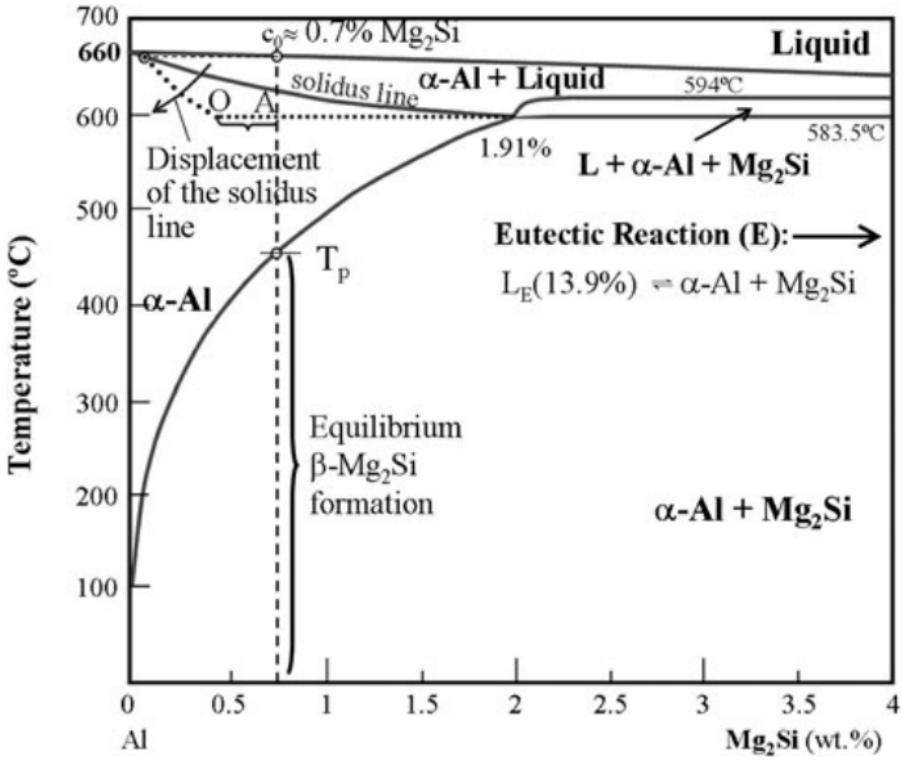

Figure 20. Pseudo-binary Al-Mg2Si phase diagram illustrating the possibility of the formation of coarse eutectic Mg2Si under non-equilibrium conditions [15,25].

4.1. Computational Modeling

Computational modeling was performed based on the concept that aluminum is indeed a heterogeneous material with at least 9 different constituents. Table 4 shows the constituents considered in the modeling. For the damage accumulation, omega ω in Equation (6) is expressed as the summation of the plastic strain.

Table 4. Constituents considered in the FEA modeling.

Name of Constituent	Modulus GPa	Poisson's Ratio	Failure Condition	Main Characteristics Related to Modeling	Ref.
Al matrix	68.0	0.30	Johnson–Cook	This can usually be model with elastoplastic	[25]
β-Mg2Si	105.0	0.29	Mises	Disrupt the homogeneity, brittle cracking failure	[26,27]
Sub GB	66.5	0.30	Johnson–Cook	Atomic mismatch stronger than the matrix	[10]
GB	67.0	0.29	Johnson–Cook	Similar with low angle with even higher UTS	[28–30]
Eutectic Mg2Si	105.0	0.29	Mises	segregation around the grain boundary also called coarse Mg2Si	[31]
β-Al5FeSi	150.0	0.28	Max strain	Disrupt the homogeneity, brittle cracking failure	[15,32]
π-$FeMg_3Si_6Al_8$	43.0	0.27	Mises	-	[20]
AlCr	111.161	0.27	Strain energy	-	[18]
Si	112.0	0.28	Strain energy	-	[24]

4.1.1. Aluminum Matrix

At room temperature, aluminum has very little solid solubility for other metals. Pure aluminum does not have a high tensile strength. However, the addition of alloying elements such as manganese, silicon, copper, and magnesium can increase the strength of aluminum and produce an alloy with properties tailored to particular applications [25].

4.1.2. Mg2Si Precipitates

Magnesium silicide is used to create aluminum alloys of the 6000 series, containing up to approximately 1.5% Mg2Si. An alloy of this group can be age-hardened to form Guinier–Preston zones and a very fine precipitate, both resulting in increased strength of the alloy. Mg2Si crystallizes in the antifluorite structure and displays a face-centered cubic lattice arrangement. In the face-centered cubic lattice, Si centers occupy the corners and face-centered positions of the unit cell and Mg centers occupy the eight tetrahedral sites in the interior of the unit cell. The coordination numbers of Si and Mg are eight and four, respectively [26,27].

4.1.3. Grain Boundary

The grain boundaries, which are closely related to the two constituents above, are the lines that divide grains that have the same crystal orientation.

This interface is also known to have atomic mismatch, and as a result it is thought to be stronger than the matrix. Small-angle grain boundaries occur when the mismatch is minor, to the order of a few degrees. The grain boundaries are also known to be more chemically reactive than the grain itself. This is also a popular spot for pollutants to congregate. There is not much research on this topic [28–30]. The grain boundary was considered to have a mechanical property of 1.05 percent that of the solid solution in this study. For the simulation, a similar failure law was used.

4.1.4. Subgrain Boundaries

Low-angle grain boundaries (LAGB) or subgrain boundaries are those with a misorientation of less than or nearly 15 degrees. LAGB are composed of a cluster of dislocations and their properties and structure are a consequence of the misorientation. The properties of high-angle grain boundaries, whose misorientation is larger than 15 degrees, are cus-

tomarily found to be independent of the misorientation. In any case, there are uncommon boundaries at particular presentations, whose interfacial energies are interestingly lower than those of common high-angle grain boundaries [10].

4.1.5. Mg2Si Eutectic (Coarse Mg2Si)

Coarse Mg2Si precipitates form under non-equilibrium solidification conditions due to the rapid cooling rates. The macrosegregation phenomena seen in alloy 6063, which can be seen in the findings of the particle volume fraction, are evidence of the process of non-equilibrium solidification [25,33].

4.1.6. β-Al5FeSi

Impurities such as iron, which is the most deleterious impurity for AlSiMg alloys, form various intermetallic compounds with Si and Mg, such as α-(Fe2SiAl8), β-(FeSiAl5), and π(FeMg3Si6Al8). Among these compounds, the formation of plate-shaped β compounds reduces the mechanical properties, particularly the ductility and fracture toughness. The size and volume fraction of the β plates depend strongly on the Fe content, solidification rate, and level of modification. The β-phase–π-phase transformation is dependent on the Mg content. The typical microstructure of as-cast 6063 contains an aluminum matrix and Fe-containing intermetallic phases of β-Al5FeSi located at the grain boundaries and Mg2Si [34,35] due to the low solubility limit of Fe, Si, and Mg in the aluminum matrix.

4.1.7. π-(FeMg3Si6Al8)

The β-phase–π-phase transformation is dependent on the Mg content. As long as β-FeSiAl5 is the Fe bearing phase, all of the Mg will be in a solid solution. Further additions of Mg will first lead to transformation of the β-AlFeSi into π-FeMg3Si6Al8, while the concentration of Mg in solid solution will stay constant [28,36].

4.1.8. AlCr

Cr was relatively uniformly distributed with a slight segregation toward the grain centers. As the solid solubility of Fe in aluminum is low (<0.05 wt%), it was beyond the resolution of the microprobe measurements [37].

4.1.9. Si Particles

The solubility of Si in Al is quite low. In wrought alloys, silicon is used with magnesium at levels up to 1.5% to produce Mg2Si in the 6xxx series of heat-treatable alloys. Dispersion particles only have a minor influence on the strength. If magnesium or silicon precipitates on them during cooling and after solution annealing, meaning the desired magnesium silicide does not form, their strength actually reduces. Silicon preferentially precipitates at the grain boundaries because it experiences nucleation problems. Magnesium silicide is also precipitated there [38,39].

4.1.10. Computational Approach

The computational approach was implemented using Abaqus^{TM} version 14 and the 3-D Model was created using a software platform for data visualization processing and analysis, Amira^{TM} version 6. The modeling was performed in two steps: global model creation and local model creation. Previous studies [40–42] employed a similar concept. The simplified notion is depicted in Figures 21 and 22. The external loads and boundary conditions can be applied via global modeling. The stress and strain values near the area of interest are then calculated using this global model. The local model is then computed using this strain result to generate the final results. This method is not as time-consuming as traditional multi-level modeling. All of the defined aluminum alloy component data values are used to model the basic microstructure. This digitized micrograph is then converted into finite element data that can be used. The boundary condition for the local model is then put up using the strain result from the global model. The modeling process began

with the building of the global model. A hole cylinder specimen was produced for this purpose. A simple strain condition was used in this simulation. A similar strategy was adopted in [43,44]. This method is effective in simulating the failure state [43].

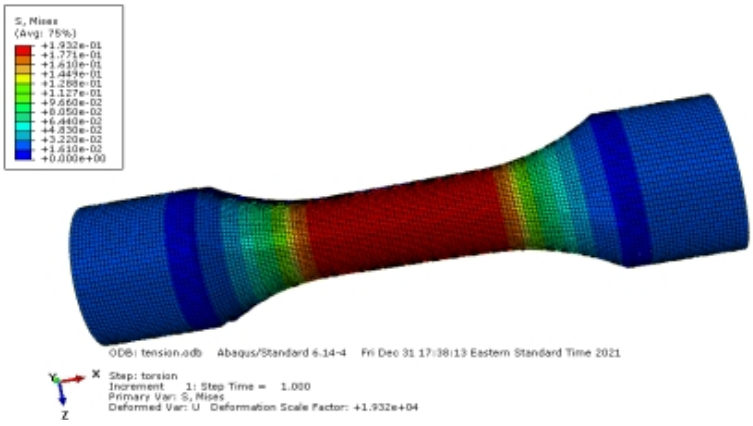

(**a**)

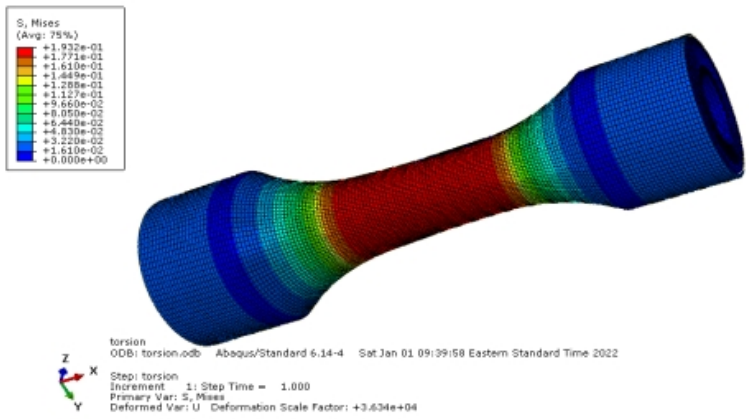

(**b**)

Figure 21. Procedure of the modeling. The local model is based on aluminum with approximate grain sizes of 6–7 ASTM GS. The square is 50 × 50 A0. (**a**) Under tension loading. (**b**) Under torsion loading.

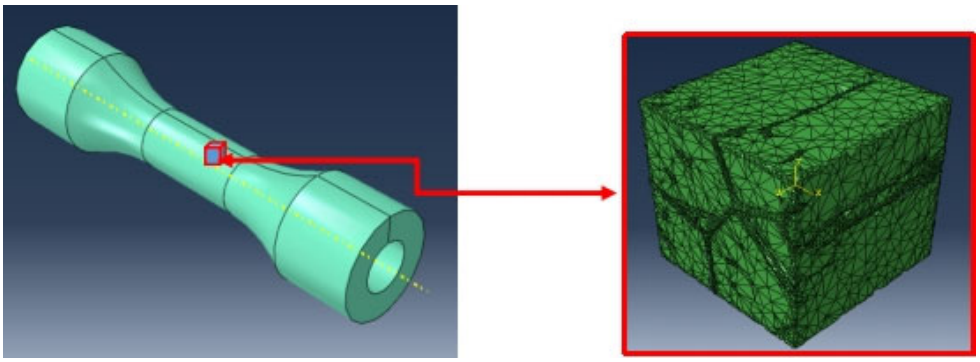

Figure 22. The micro model is embedded into the macro model and a linkage is than established.

The sample for the global model in this study was a thin-walled tubular specimen with a wall thickness of 1.5 mm. The cylinder bore was 18 mm in diameter. The analysis took several minutes to complete in an explicit context. The global model's output was then exported to the local model, which was built with Amira^{TM}. We were able to replicate

it efficiently by using the strain results from the global model as the boundary conditions for the local model. There is a more in-depth explanation of the modeling technique elsewhere [26]. The stress distribution is the final product. Individual mechanisms are used to create the model's failure mechanism. The Johnson–Cook model is utilized for solid solutions, twin boundaries, grain boundaries, and the aluminum matrix. A similar study [40,45] was also published.

The damage accumulation x, which is the sum of the plastic strain, is expressed using Equations (6) and (7) [41,42]:

$$\omega = \sum \left(\frac{\Delta \bar{\varepsilon}^{pl}}{\Delta \bar{\varepsilon}_f^{pl}} \right) \tag{6}$$

The plastic strain is determined as follows:

$$\Delta \bar{\varepsilon}_f^{pl} = \left[d_1 + d_2 exp\left(d_3 \frac{p}{q} \right) \right] \left[1 + d_4 ln \frac{\bar{\varepsilon}^{pl}}{\bar{\varepsilon}_0} \right] \tag{7}$$

where p denotes pressure and q denotes von Mises stress. Damage parameters d_1 and d_4 are 0.13, 0.13, 1.5, and 0.011, respectively [46,47]. The maximum stress–strain rule was applied to the brittle constituents:

$$\overline{\epsilon} = \overline{\epsilon}_{crit} \tag{8}$$

or:

$$\overline{\sigma} = \overline{\sigma}_{crit} \tag{9}$$

4.2. From the Standpoint of Mechanics

The global model's results are displayed in Figure 21. The assumption behind this model is that the material is homogeneous. The local models are inserted right at the surface. The findings of the static analysis or stress distribution when the sample is subjected to slow and small loading or when the sample is in a static condition, where stress does not cause any damage, are shown in Figures 22 and 23. These conditions show the difference between tension and torsion when they are implemented separately. Although the stresses concentrate around the hard elements, the figures indicate that at low stress levels, they are not harmful. We note the fact that Figure 23 in reality is modeling one unit cell consisting of only one grain. In Figure 23, the unit cells were simply loaded with tension (Figure 23a) and torsion (Figure 23b). It shows the stress distribution within the unit cell. Also note that despite their simple loadings, the distribution within the unit cells is obvious. In Figure 23a, the stress is concentrated on and around the grain boundary, while that does not happen in Figure 23b.

By embedding the unit cell inside the macro model, a more realistic model can be achieved. For the failure theory, the stress and strain relation follow the Johnson–Cook model, namely as the following:

$$\sigma^0 = \left[A + B(\varepsilon^p)^n \right] \cdot \left(1 + C \cdot ln\left(\frac{\bar{\varepsilon}^{pl}}{\bar{\varepsilon}_0} \right) \right) \cdot \left(1 - \hat{T}^m \right) \tag{10}$$

where $\hat{T}^m$ is the homologous temperature.

Figure 24 shows the prediction of the crack path based on the amount of damage. The dark element shows that the cracking has taken place to follow Equations (8) and (9). With these being stitches, it would be similar to Figure 14.

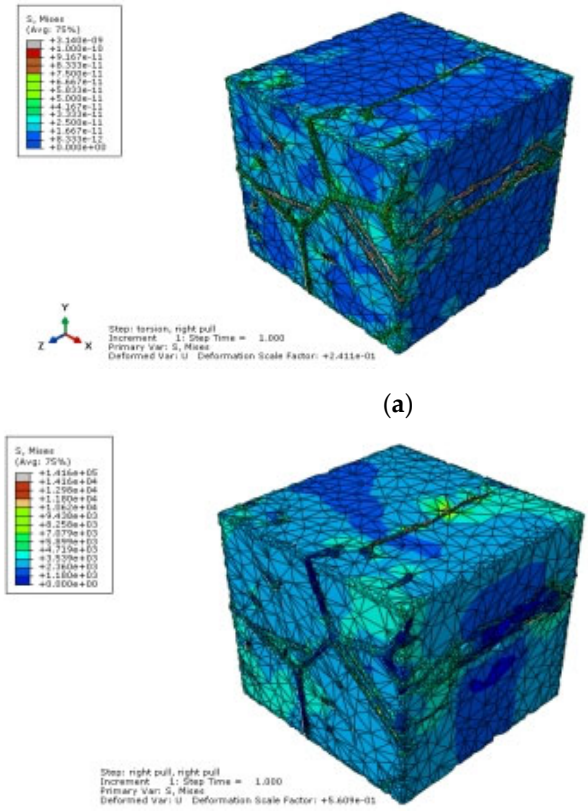

Figure 23. (**a**) The micro model: embedded in tension; (**b**) embedded in torsion.

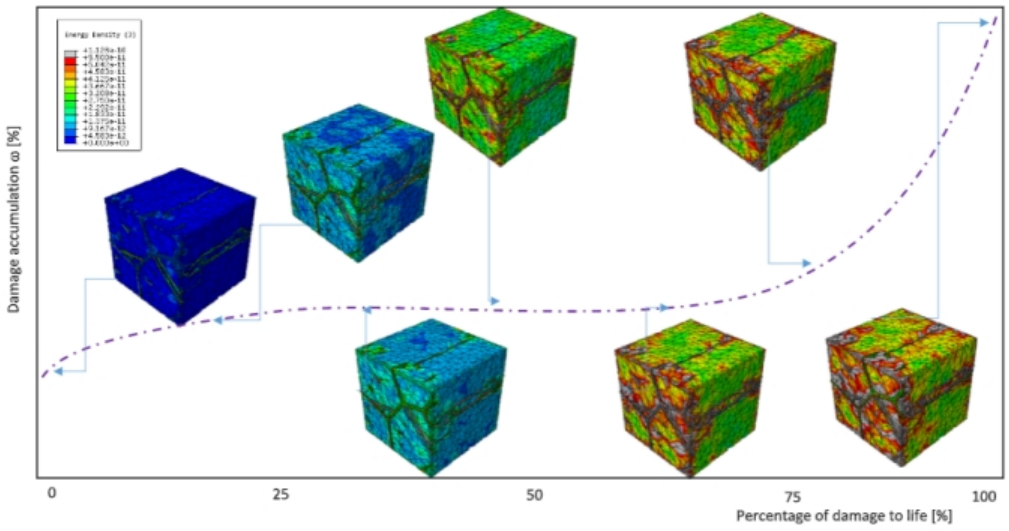

Figure 24. Damage map due to fatigue.

In general, from a mechanical standpoint, cracking tends to start around the hard particles such as β-Mg5Si, Si, Al, and Cr in all locations, starting from the left edges, through the solid solution towards the grain boundary, and then to the grain boundary, where the silica resides in this case. It then moves on to a location near the *p* or β-Al5FeSi. Because of the elongated shape the cracking is perpendicular to the primary loading axis in the macro model. On the other hand, the main matrix provides some flexibility in terms of generating high damage. It is, however, not as significant as the other hard components. Inclusions that are parallel to the primary loading axis have less influence than inclusions

that are elongated perpendicular to it. This fact is in line with the fundamental principles of fracture mechanics. The form of the particles, the strain rate, and the matrix failure law are the three factors that influence the situation.

4.3. From a Metallurgical Standpoint

Microstructural factors have long been known to influence the material and mechanical properties, as shown in [46,47]. Alloying elements and heat treatments cause these property changes, and as a result cause microstructural changes [48–52]. Normally, it is assumed that a metal's fracture toughness improves as its tensile strength drops, based on room-temperature test data. An increased grain boundary density increases the lifetime of the materials because it delays the crack development along the stress line [53–55]. However, in order to avoid creep difficulties, the operating temperature must be below 0.3 Tm. The grain boundaries tend to slide at elevated temperatures, which can cause the materials to fail [56–59].

4.4. Experimentation-Based Verification

It will take some time for us to confirm this conclusion through experimentation. This is scheduled to take place in the near future, depending on the circumstances. Fortunately, similar articles on this subject are available, although not in abundance, and are included here for the reader's convenience [60–64]. It has been experimentally verified that the elements have no deleterious effect at mild stress levels. Harder constituents, on the other hand, are advantageous due to their higher load-carrying capacities [46,48,49,61,63,64]. Experimental verification data are shown in Figure 8 [62]. In the illustration, the aluminum contains certain microstructural alterations (see the TEM micrograph in the figure), which is the d-ferrite formation. The image also indicates that the fracture nucleation and propagation are highly dependent on the constituents and are heavily influenced by the shapes and failure laws.

5. Conclusions

From the experimental and computational results, the following conclusions can be drawn:

- Most of the initial fatigue cracks are found in planes parallel to the maximum shear stress. Based on the experimental results, a crack propagation model can be proposed by following the laws of crack mechanics, starting with the cracks in the plane with the maximum shear stress;
- The initial cracks are mostly found in planes parallel to the maximum shear stress. Statistically, the microcracks under tension modes are highest at 45° (approximately 30%), while under torsion are highest at 0° (approximately 20%) with respect to the sample orientation. The influence of the microstructure is explained by finite element analysis;
- The initial cracks not only propagate on the surface but also propagate towards the inside of the material;
- With the application of SEM, it is possible to find crack propagation that is hampered by the microstructural barriers;
- The stress distribution and cracking in the AlMgSi were both modeled. The model took into account the load-carrying function's constituent phases. The calculation results from the specimen were used as inputs for the boundary conditions. The local models were positioned on the surface. Hard and soft materials are treated differently in the models, with various failure rules. The findings suggest that the constituents and the microstructure have a crucial role in increasing the material strength at low stress levels, analogous to the hard fibers of a composite material. The hard and especially sharp elements, on the other hand, become damaging to the system as the stress increases to the point where cracking can occur. They serve as a starting point for cracking. This discovery corresponds to what is known in the field of metallurgy.

Three mechanical parameters influence the cracking conditions, namely the particle form (microstructure), strain rate, and matrix failure law.

Author Contributions: Conceptualization, H.A.S., K.K. and Y.P.; methodology, H.A.S., Y.P. and K.K.; software, Y.P. and H.A.S.; validation, H.A.S., K.K. and Y.P.; formal analysis, H.A.S., K.K. and YP.; investigation, H.A.S., K.K. and Y.P.; resources, H.A.S., K.K. and Y.P.; data curation, H.A.S., K.K. and Y.P.; writing—original draft preparation, H.A.S. and Y.P.; writing—review and editing, H.A.S., K.K. and Y.P.; visualization, H.A.S., K.K. and Y.P.; supervision, H.A.S., K.K. and Y.P.; project administration, H.A.S., K.K. and Y.P.; funding acquisition, HAS, K.K. and Y.P. All authors have read and agreed to the published version of the manuscript.

Funding: This research received no external funding.

Institutional Review Board Statement: Not applicable.

Informed Consent Statement: Not applicable.

Data Availability Statement: Data sharing not applicable.

Acknowledgments: The authors would like to thank to H. Zenner, Deutschen Akademischen Austauschdienst, IMAB and ISAF TU Clausthal, and DFG for the support and K. Poetter, A. Schram, V. Duewel, H. Mauch and F. Youssefi-Hashtyani for the numerous constructive discussions and collaborative work.

Conflicts of Interest: The authors declare no conflict of interest.

References

1. Eulitz, K.-G.; Döcke, H.; Esderts, A.; Kotte, K.L.; Zenner, H. *Lebensdauervorhersage II, Verbesserung der Lebensdauerabschätzung durch systematische Aufarbeitung und Auswertung vorliegender Versuchsdaten, Forschungskuratorium Maschinenbau, 227*; FKM: Frankfurt, Germany, 1997.
2. Zenner, H. *Lebensdauerkonzepte, Beschreibung-Kritik-Entwicklungen, in Fatigue Life Concepts, Description—Review—Developments*; DVM: Berlin, Germany, 1997.
3. Wang, Q.; Berard, J.Y.; Rathery, S.; Bathias, C. High-cycle fatigue crack initiation and propagation behaviour of high-strength spring steel wires. *Fatigue Fract. Eng. Mater. Struct.* **2003**, *22*, 673–677. [CrossRef]
4. Murakami, Y. What is fatigue damage? A viewpoint from the observation of a low-cycle fatigue process. In *Metal Fatigue*; Academic Press: Cambridge, MA, USA, 2019.
5. Murakami, J.; Miller, K.J. What is Fatigue Damage? A View Point from the Observation of Low Cycle Fatigue Process. *Int. J. Fatigue* **2005**, *27*, 991–1005. [CrossRef]
6. Mbuyaa, T.O.; Gub, Y.; Thomson, R.C.; Reed, P.A.S. Effect of intermetallic particles and grain boundaries on short fatigue crack growth in a cast Al–4Cu–3Ni–0.7Si piston alloy. *Fatigue Fract. Eng. Materals Struct.* **2017**, *40*, 1428–1442. [CrossRef]
7. Liu, G.; Winwood, S.; Rhodes, K.; Birosca, S. The Effects of Grain Size, Dendritic Structure and Crystallographic Orientation on Fatigue Crack Propagation in IN713C Nickel-Based Superalloy. *Int. J. Plast.* **2020**, *125*, 150–168. [CrossRef]
8. Fleishel, R.; Cauthen, C.; Daniewicz, S.; Baker, A.; Jordon, B.; TerMaath, S. Characterization of Surface Fatigue Crack Nucleation and Microstructurally Small Crack Growth in High Strength Aluminum Alloys. *Front. Mater.* **2021**, *7*, 590747. [CrossRef]
9. Carpinteri, A. *Handbook of Crack Propagation in Metallic Structures*; Elsevier: Amsterdam, The Netherlands, 1994.
10. Gottstein, G. *Physical Foundations of Materials Science*; Springer: Berlin, Germany, 2014.
11. Husein, S. Crystal Structure of Metals. In *Metalurgy*; University of Baghdad: Baghdad, Iraq, 2019; pp. 1–25.
12. Soboyejo, W. *Mechanical Properties-of-Engineered-Materials, Crystal Stucture and Dislocation Motion*; Marcel Dekker Inc.: New York, NY, USA, 2002.
13. Zhang, Y.H.; Edward, L. On the blocking effect of grain boundaries on small crystallographic fatigue crack growth. In *Materials Science and Engineering*; Elsevier: Amsterdam, The Netherlands, 1994; Volume A188, pp. 121–123.
14. Asensiio-Lozano, J.; Pena, J.S.; Vander Voort, G.F. Effect of Processing Steps on the Mechanical Properties and Surface Appearance of 6063 Aluminium Extruded Products. *Materials* **2014**, *7*, 4224–4242. [CrossRef]
15. Vander Voort, G.; Suarez-Pena, B.; Asensio-Lozano, J. *Microstructure Investigations of Streak Formation in 6063 Alumunium Extrusions by Optical Metallographic Techniques, Microscopy and Microanalysi*; Cambridge University Press: Cambridge, UK, 2013.
16. Dedov, S.; Lehmann, G.; Kawalla, R. *Application of Combined Casting-Forging Process for Production of Durable Lightweight Aluminum Parts, Key Engineering Materials*; Scientific Nets: Kapellweg, Switzerland, 2013; Volume 554–557.
17. Polák, J.; Mazanova, V.; Heczko, M.; Petráš, R. *The Role of Extrusions and Intrusions in Fatigue Crack Initiation, Engineering Fracture Mechanics*; Elsevier: Amsterdam, The Netherlands, 2017; Volume 185, pp. 46–60.
18. Hopson, P.D.; Brown, M.W.; De Los Rios, E.R. *Two Phases of Short Crack Growth in Medium Carbon Steel*; EGF Pub: London, UK, 1986; Volume 1, pp. 441–459.

19. Miller, K.J. *Multiaxial Fatigue: A Review, Schaedigungsfrueherkenung und Schadensablauf bei metalischen Bauteilen*; DVM: Darmstadt, Germany, 1993.
20. Plumbridge, W.J. Review: Fatigue Crack propagation in metallic and polymeric materials. *J. Mater. Sci.* **1972**, *7*, 939–962. [CrossRef]
21. Issler, L.; Ruos, H.; Haefele, P. *Fesfigkeitslehre Grundlagen*; Springer: Berlin, Germany, 2013.
22. Gancarz, T.; Jourdan, J.; Gasior, W.; Henein, H. Physicochemical properties of Al, Al-Mg and Al-Mg-Zn Aloys. *J. Mol. Liq.* **2018**, *249*, 470–476. [CrossRef]
23. Li, H.; Cao, F.; Guo, S.; Jia, Y.; Zhang, D.; Liu, Z.; Wang, P.; Scudino, S.; Sun, J. Effects of Mg and Cu on microstructures and properties of sprays-deposited Al-Zn-Mg-Cu alloys. *J. Alloy. Compd.* **2017**, *719*, 89–96. [CrossRef]
24. Rodríguez, S.V.; Martínez, L.; Pech-Canul, M. Solidification Physics and Microstructure: A Study of AlMg and AlMgSi Alloys by Vortex Method. [pengar. buku] Alicia Esther Ares. In *Solidification*; Intechopen: London, UK, 2018. [CrossRef]
25. Davis, J.R. *ASM Specialty Handbook: Alumunum and Alumimum Alloys*; ASM International: Materials Park, OH, USA, 2001; pp. 352–416.
26. Monteiro, W.A.; Espósito, I.M.; Ferrari, R.B.; Buso, S.J. Microstructural and Mechanical Characterization after Thermomechanical Treatments in 6063 Aluminum Alloy. *Mater. Sci. Appl.* **2011**, *2*, 1529–1541. [CrossRef]
27. ASM Handbook Committee. *Properties and Selection: Non-ferrous Alloys and Special Purpose Materials*; ASM International: Materials Park, OH, USA, 1990.
28. Tan, L.; Sridharan, K.; Allen, T.; Nanstad, R. Microstructure tailoring for property improvements by grain boundary engineering. *J. Nucl. Mater.* **2008**, *374*, 270–280. [CrossRef]
29. Shimada, M.; Kokawa, H.; Wang, Z.J.; Sato, Y.S.; Karibe, I. Optimization of grain boundary character distribution for intergranular corrosion resistant 304 stainless steel by twin-induced grain boundary engineering. *Acta Mater.* **2002**, *50*, 2331–2341. [CrossRef]
30. Sharmaa, P.; Ganti, S. On the grain-size-dependent elastic modulus of nanocrystalline materials with and without grain-boundary sliding. *J. Mater. Res.* **2003**, *18*, 1267–1279. [CrossRef]
31. Asensio-Lozano, J.; Van der Voort, G. *The Al-Si Phase Diagram*; Technical Note; Buehler, a Division of Illinois Tool Works: Waukegan Road Lake Bluff, IL, USA, 2015; Volume 5, p. 1.
32. Castillo-Hernande, G.; Yasseri, M.; Klobes, B.; Ayachia, S.; Müller, E.; de Boor, J. Room and high temperature mechanical properties of Mg2Si, Mg2Sn and their solid solutions. *J. Alloy. Compd.* **2020**, *845*, 156205. [CrossRef]
33. Gruzlesky, J.E. *Segregation phenomena: In Microstructure Development during Metalcasting*; American Foundy Society Inc.: Schaumburg, IL, USA, 2000; pp. 117–131.
34. Kliauga, A.M.; Vieira, E.A.; Ferrante, M. The influence of impurity level and tin addition on the ageing heat treatment of the 356 class alloy. *Mater. Sci. Eng.* **2008**, *480*, 5–16. [CrossRef]
35. Zajac, S.; Hutchinson, B.; Johansson, A.; Gullman, L.O. Microstructure control and extrudability of Al-Mg-Si alloys microalloyed with manganese. *Mater. Sci. Technol.* **1994**, *10*, 323–333. [CrossRef]
36. AlMgSi Alloys. Total Materia, The World's Most Comprehensive Materials Database. Available online: https://www.totalmateria.com/page.aspx?ID=Home&LN=EN (accessed on 16 April 2022).
37. Kenyon, M.; Robson, J.; Fellowes, J.; Liang, Z. *Effect of Dispersoids on the Microstructure Evolution in Al-Mg-Si Alloys; Advance Engineering Materia*; lWILEY-VCH Verlag GmbH & Co.: Weinheim, Germany, 2019; Volume 1800494, pp. 1–7.
38. Ostermann, F. *Andungstechnologie Aluminium*; Springer: Berlin, Germany, 2014.
39. Zainon, F.; Ahmad, K.R.; Daud, R. Effect of intermetallic phase on microstructure and mechanical properties of AA332/Mg2Si(p) composite. *AIP Conf. Proc.* **2017**, *1835*, 020043. [CrossRef]
40. Prawoto, Y.; Martin-Fanone, M.; Shahedi, S.; Ismail, M.S.; Nik, W.S.W. Computational approach using Johnson–Cook model on dual phase steel. *Comput. Mater. Sci.* **2012**, *54*, 48–55. [CrossRef]
41. Johnson, G.; Cook, W. A constitutive model and data for metals subjected to large strains, high strain rates and high temperatures. In Proceedings of the 7th International Symposium on Ballistics, Hague, The Netherlands, 19–21 April 1983; pp. 541–547.
42. Johnson, G.; Cook, W. Fracture Characteristics of Three Metals Subjected to Various Strains, Strain Rates, Temperatures and Pressures. *Eng. Fract. Mech.* **1985**, *21*, 31–48. [CrossRef]
43. Prawoto, Y. Designing steel microstructure based on fracture mechanics approach. *Mater. Sci. Eng. A* **2009**, *507*, 74–86. [CrossRef]
44. Prawoto, Y.; Idris, R.; Kamsah, N.; Tamin, N. Two-dimensional modeling to compute plastic zone in front of compact tension sample of a multiphase material. *Comput. Mater. Sci.* **2009**, *47*, 482–490. [CrossRef]
45. Chen, A.; Ruan, H.H.; Wang, J.; Chan, H.L.; Li, Q.; Lu, J. The influence of strain rate on the microstructure transition of 304 stainless steel. *Acta Mater.* **2011**, *59*, 3697–3709. [CrossRef]
46. Lee, W.-S.; Lin, C.-F. Impact properties and microstructure evolution of 304L stainless steel. *Mater. Sci. Eng.* **2001**, *308*, 124–135. [CrossRef]
47. Sen, I.; Amankwah, E.; Kumar, N.S.; Fleury, E.; Oh-ishi, K.; Hono, K.; Ramamurty, U. Microstructure and mechanical properties of annealed SUS 304H austenitic stainless steel with copper. *Mater. Sci. Eng.* **2011**, *528*, 4491–4499. [CrossRef]
48. Salahinejad, E.; Amini, R.; Hadianfard, M. Structural evolution during mechanical alloying of stainless steels under nitrogen. *Powder Technol.* **2012**, *215*, 247–253. [CrossRef]
49. Martin, M.; Weber, S.; Theisen, W.; Michler, T.; Naumann, J. Development of a stable high-aluminum austenitic stainless steel for hydrogen applications. *Int. J. Hydrog. Energy* **2011**, *36*, 15888–15898. [CrossRef]

50. Fatahalla, A.; Abu Elezz, N.A.; Semeida, M. Experimental characterization of a Si–Mo–Cr ductile cast iron. *Mater. Sci. Eng.* **2009**, *504*, 81–89. [CrossRef]
51. Wang, Y.D.; Tang, H.B.; Fang, Y.L.; Wang, H.M. Effect of heat treatment on microstructure and mechanical properties of laser melting deposited 1Cr12Ni2WMoVNb steel, Mater. *Sci. Eng. A* **2010**, *528*, 474–479. [CrossRef]
52. Isfahany, A.N.; Saghafian, H.; Borhan, G. The effect of heat treatment on mechanical properties and corrosion behavior of AISI420 martensitic stainless steel. *J. Alloy. Compd.* **2011**, *509*, 3931–3936. [CrossRef]
53. Szabo, P.J. Effect of partial recrystallization on the grain size and grain boundary structure of austenitic steel. *Mater. Charact.* **2012**, *66*, 99–103. [CrossRef]
54. Gavriljuk, V.; Berns, H.; Escher, C.; Glavatskaya, N.I.; Sozinov, A.; Petrov, Y.N. Grain boundary strengthening in austenitic nitrogen steels. *Mater. Sci. Eng. A* **1999**, *271*, 14–21. [CrossRef]
55. Mishin, O.; Gertsman, V.Y.; Alexandrov, I.V.; Valiev, R.Z. Grain boundary character distributions and mechanical properties of 304 stainless steel1, Mater. *Sci. Eng. A* **1996**, *212*, 281–283. [CrossRef]
56. Sauzay, M. Modelling of the evolution of micro-grain misorientations during creep of tempered martensite ferritic steels. *Mater. Sci. Eng. A* **2009**, *74–80*, 510–511.
57. Woo, N.S. Assessment of damage and life prediction of austenitic stainless steel under high temperature creep–fatigue interaction condition. *Mater. Sci. Eng. A* **2002**, *322*, 64–72.
58. Chen, B.; Flewitt, P.E.J.; Smith, D.J.; Jones, C.P. An improved method to identify grain boundary creep cavitation in 316H austenitic stainless steel. *Ultramicroscopy* **2011**, *111*, 309–313. [CrossRef]
59. Spigarelli, S.; Cabibbo, M.; Evangelista, E. Analysis of the creep strength of a low-carbon AISI 304 steel with low-Σ grain boundaries, Mater. *Sci. Eng. A* **2003**, *352*, 93–99. [CrossRef]
60. Lo, K.; Shek, C.; Lai, J. Stainless steels: An introduction and their recent developments. *Mater. Sci. Eng. R Rep.* **2009**, *65*, 39–104. [CrossRef]
61. Bugat, S.; Besson, J.; Pineau, A. Micromechanical modeling of the behavior of duplex stainless steel. *Comput. Mater. Sci.* **1999**, *16*, 158–166. [CrossRef]
62. Alvarez-Armas, I.; Marinelli, M.C.; Malarrı, J.A.; Degallaix, S.; Armas, A.F. Microstructure associated with crack initiation during low-cycle fatigue in a low nitrogen duplex stainless steel. *Int. J. Fatigue* **2007**, *29*, 758–764. [CrossRef]
63. Iacoviello, F. Microstructure influence on fatigue crack propagation in sintered stainless steels. *Int. J. Fatigue* **2005**, *27*, 155–163. [CrossRef]
64. Das, A.; Tarafder, S. Experimental investigation on martensitic transformation and fracture morphologies of austenitic stainless steel, Int. *J. Plasticity* **2009**, *25*, 2222–2247. [CrossRef]